Available online at www.sciencedirect.com

jmr&t Journal of Materials Research and Technology

journal homepage: www.elsevier.com/locate/jmrt

Original Article

Experimental assessment of low-temperature martensite transformations in Ni-rich polycrystalline Ni–Ti alloys

Ariel Moreno-Gobbi [a], *Paulo Sergio Silva Jr.* [b], *Diego Rafael Nespeque Correa* [c,g], *Alfredo Masó Milá* [a], *Javier Andrés Muñoz Chaves* [d,e], *Carlos Roberto Grandini* [f,g], *Rafael Formenton Macedo dos Santos* [d,e], *Conrado Ramos Moreira Afonso* [d,e,*]

[a] *Laboratorio de Acústica Ultrasonora, Instituto de Fisica, Facultad de Ciencias, UdelaR. Iguá 4225, Montevideo, Uruguay*

[b] *Department of Physics, Federal University of São Carlos (UFSCar), 13565-905 São Carlos, SP, Brazil*

[c] *IFSP - Federal Institute of Education, Science, and Technology, Grupo de Pesquisa Em Materiais Metálicos Avançados, 18095-410, Sorocaba, SP, Brazil*

[d] *Graduate Program in Materials Science and Engineering (PPG-CEM), Federal University of São Carlos (UFSCar), 13565-905 São Carlos, SP, Brazil*

[e] *Department of Materials Engineering (DEMa), Federal University of São Carlos (UFSCar), 13565-905 São Carlos, SP, Brazil*

[f] *Laboratório de Anelasticidade e Biomateriais, UNESP - Universidade Estadual Paulista, Bauru, SP, 17.033-360, Brazil*

[g] *IBTN/BR - Brazilian Branch Institute of Biomaterials, Tribocorrosion and Nanomedicine, Bauru, SP, 17.033-360, Brazil*

ARTICLE INFO

Article history:
Received 12 February 2022
Accepted 20 April 2022
Available online 30 April 2022

Keywords:
Ni–Ti alloy
Ultrasonic characterization
Martensitic transformations
Cryogenic temperature
Thermal properties

ABSTRACT

Ultrasonic velocity and attenuation measurements of a commercially available Ni-rich polycrystalline Ni–Ti alloy were simultaneously obtained upon cooling from room temperature (RT) down to 130 K. The anelastic spectra show multiple anomalies in both velocity and attenuation curves, which evidence a complex nature of structural rearrangements exhibited by Ni–Ti alloy, associated with relaxations and phase transformations. In particular, some evident anomalies at **285 and 180 K**, not previously exploited using ultrasonic measurements on Ni-rich polycrystalline Ni–Ti alloy, were associated with austenite to pre-martensitic (B2 → R) and pre-martensitic to martensitic (R → B19') phase transitions, respectively. The peculiar temperature separation between these transformations was interpreted based on chemical composition and the Ni–Ti alloy microstructure evolution. **X-ray diffraction (XRD), scanning electron microscopy (SEM) and differential scanning calorimetry (DSC)** were also used to add complementary results about phase transformations and thermal events exhibited by Ni–Ti alloy at low temperatures.

* Corresponding author.
E-mail address: conrado@ufscar.br (C.R. Moreira Afonso).

https://doi.org/10.1016/j.jmrt.2022.04.096

XRD, Rietveld refinement, SEM and **transmission electron microscopy (TEM)** analyses confirm the coexistence of the austenite B2, martensite B19', and Ni_4Ti_3 phases at RT. DSC measurements indicated reversible two-stage martensitic transitions involving B2 ↔ R ↔ B19' phase transformations at similar temperatures than the observed from ultrasonic anomalies. Besides that, several anelastic relaxation events identified around the phase transitions reveal the occurrence of complex physical mechanisms, such as accommodation of the twinned R-phase and martensite domain walls, twinning boundaries mobility, and the coupling between stress-induced dislocation motion and interstitial diffusion, not reported simultaneously in the literature. The ferroelastic nature of martensite and pre-martensite phase transformations was confirmed for a commercially available Ni-rich polycrystalline Ni–Ti alloy studied in this work.

1. Introduction

In the last decades, **titanium (Ti)** and its alloys have received considerable attention as biomedical materials used in load-bearing implants such as artificial hip joints, bone plates and screws, spinal instruments, and dental implants [1]. The main advantages of **Ti-based** alloys are good biocompatibility, relatively low elastic modulus, excellent corrosion resistance, and, particularly, good strength to density ratio [2–6]. The influence of alloying elements on **Ti** alloys contributes to a wide range of microstructural and mechanical properties [7]. The mechanical properties of **Ti** are determined by its degree of purity, which fundamentally depends on the production and processing conditions [8]. The presence of impurities in determined amounts increases hardness and strength to the detriment of plasticity. The increased affinity of **Ti** determines the presence of impurities like oxygen, nitrogen, carbon, and hydrogen at high temperatures [7]. Among Ti-based alloys, Ti-50at.%Ni (Nitinol) [9] is one of the most promising **Ti** implants as it possesses a mixture of novel properties such as shape memory effect, suitable biocompatibility, superelasticity, and high damping properties. Their medical applications include orthodontic wires for dental, intravascular stents, bone fracture fixtures, and staples for foot surgery.

Ni–Ti-based alloys are the most important commercial shape memory alloys with excellent mechanical properties [10–12]. The matrix comprises the TiNi austenite phase, with a B2 ordered structure (CsCl-type) at **room temperature (RT)**, the martensite is named B19' (monoclinic), and the martensitic transformation occurs in two or more steps. Usually, the first transformation is characterized by minimal temperature hysteresis called "R-phase transformation", which is considered a pre-martensitic behavior (precursor effect) before the subsequent martensitic transformation itself. The second transformation is characterized by a large temperature hysteresis and represents the subsequent transformation from R-phase to B19' phase [13].

According to Otsuka and Wayman [14], Ni–Ti alloys are pseudoelastic at **RT**, while the precipitates formation can occurs at different temperatures [14–16]. Among these Ni-rich precipitates, Ni_4Ti_3 is formed at lower aging temperatures and shorter aging times [16]. While Ni_3Ti is formed at higher aging temperatures and longer times, and Ni_3Ti_2 is formed at intermediate aging temperatures and times [17]. The lenticular structured Ni_4Ti_3 intermetallic phase is the most relevant concerning shape memory characteristics such as transformation transition temperatures, the occurrence of residual strains, plastic yield limit, hysteresis size, and transformation and reorientation slopes [15]. As the final mechanical properties of Ni–Ti-based alloys are susceptible to microstructural features, controlling the microstructural evolution during thermomechanical processing is of significant importance.

Elastic energy dissipation spectra (attenuation or internal friction) and anelastic relaxation form the mechanical spectroscopy method core, widely used in solid-state physics, physical metallurgy, and materials science, to study structural defects and their mobility, transport phenomena, and phase transformations in solids [18]. In wave-propagation experiments, short high-frequency pulses (frequency about MHz or even more) are propagated through the sample [19], and their velocity and attenuation are monitored as a function of the temperature in the sample. It is well known that the conventional ultrasonic pulse-echo technique is very sensitive to the structural changes of the material [20], especially to linear defects [21], domain walls motion [22], and phase transitions [23,24].

Currently, the low-temperature effects on the mechanical properties of Ni–Ti **shape memory alloys (SMA)** have attracted significant scientific and technological interest due to the improvements provided on their machinability [25], microhardness [26], yield and tensile strengths [27], cutting efficiency and wear resistance on the endodontic instruments [28,29]. Ultrasonic attenuation studies of low-temperature martensitic transformations in Ni–Ti alloys available in the literature are majority devoted to analyzing high purity equiatomic Ni–Ti single crystals [30–33] behavior. These studies reported ultrasonic attenuation peaks and **minima** in the velocity wave curve around the martensitic transformation temperatures. Matsumoto et al. [30] and Ren et al. [32] reported the broad ultrasonic attenuation peaks in their studies at the same temperature range of martensitic transformation, which was regarded as new features of the transformation in Ni–Ti alloys, like as evolution of martensite

domains (phase boundaries and martensite twin boundaries) during the martensite phase growth. The contribution of other physical mechanisms to the equiatomic Ni–Ti single-crystal low-temperature ultrasonic attenuation spectrum was also reported, as the martensite twin boundary motion, which gave place to relaxation peaks below the martensite–austenite transition temperature [32].

Delgadillo-Holtfort et al. [34] investigated the multistage martensitic transformations in aged Ni–Ti SMA with 50.8 at.% Ni using the ultrasonic pulse-echo technique at low temperatures. They reported that the temperature evolution of the shear and longitudinal elastic constant delivers valuable information on the influence of lattice inhomogeneities on the structural phase transitions in the shape memory alloy, being the dislocations and Ni_4Ti_3 precipitates the most important defect structures. The influence of the defects on the elastic properties and the structural transitions seem to be strongly altered by aging and thermal cycling. Despite that, the physical mechanism details, which contribute to the elastic properties evolution of commercial Ni-rich polycrystalline Ni–Ti alloys during ultrasonic experiments under a cryogenic environment, are still so far to be completely understood.

This work aimed to investigate the low-temperature physical mechanisms associated with reversible martensitic transformations in Ni-rich polycrystalline Ni–Ti alloy studied by the conventional ultrasonic pulse-echo technique, with longitudinal waves of frequencies 5 and 10 MHz. Characterization techniques such as **X-ray diffraction (XRD), scanning electron microscopy (SEM), transmission electron microscopy (TEM) and differential scanning calorimetry (DSC)** were also used to add complementary results regarding phase transformations, thermal events, ultrasonic attenuation and velocity measurements.

2. Materials and methods

The Ni–Ti wires with 8 mm of diameter were provided by the Nitinol Devices & Components (www.nitinol.com), with the nominal chemical composition of 54.5–57 Ni, 0.05 N + O, 0.05 Co, 0.01 Cr, 0.01 Cu, 0.05 Fe, 0.025 Nb, 0.05H (wt.%), and 500 ppm of C and O. These wires were manufactured according to industry standards ASTM F2063[9] by precise control of the composition, cold work and continuous strain-age annealing a temperature range of 720–820 K under a stress of 35–100 MPa [35].

The crystalline structure was evaluated at **RT by XRD** in the Bragg–Brentano geometry, using a Bruker D8 Advance ECO equipment, with Cu-K_α radiation ($\lambda = 1.54056$ Å). The crystalline phases were analyzed by the Rietveld method, using GSAS® software [36] and EXPGUI® interface [37], with a Y_2O_3 standard sample for instrumental contribution, and crystallographic datasheets from the **inorganic crystal structure database (ICSD)**. The microstructure was evaluated by **SEM**, using FEI Inspect S-50, equipped with an X-ray energy dispersive spectroscopy detector (EDAX SDD Apollo X). **The TEM analysis was performed** using an FEI Tecnai G2 F20 TEM/STEM 200 kV equipped with field emission gun (FEG) coupled to energy dispersive spectrometry (EDS) EDAX detector, carrying semi-quantitative analyses. The chemical analysis was performed by energy dispersive X-ray fluorescence spectroscopy (XRF), using Shimadzu EDX-720 equipment. The thermal analysis was performed by **DSC** in a NETZSCH DSC 200 F3 Maia, using **Al** crucibles containing samples weighing 12 mg at heating/cooling rates of 10 K/min, in the temperature range of 120–300 K (similar to the used for ultrasonic measurements, discussed below). The Ni–Ti sample used on the DSC characterizations was previously subjected to a chemical etching using an aqueous solution of nitric acid and hydrofluoric acid at 1:1:2 ($HF:HNO_3:H_2O$) ratio for 15 s to prevent undesired effects from sample surface impurities (oxide layers).

For ultrasonic pulse-echo measurements, one sample was cut from the original ingot as a cylinder of 10 mm diameter and 12 mm in height. The two plane faces were mechanically polished for ultrasonic measurements described in previous work [38]. Ultrasonic attenuation and velocity were measured simultaneously using the conventional pulse-echo method [20]. A MATEC ultrasonic pulse generator was employed with a liquid nitrogen cryostat, being the experiment setup completely automated for measurements and temperature heating/cooling rates monitoring. X-cut quartz ultrasonic transducers of 5 MHz and 10 MHz fundamental frequency were bonded to the sample face with Nonac Stopcock Grease. The absolute round trip time for the ultrasonic wave was initially determined between two consecutive echoes, and then the variations of the round trip time were accurately measured using cross-correlation techniques over a selected echo. Ultrasonic attenuation was obtained by monitoring two echoes in video mode, comparing the areas between two selected echoes. Measurements were firstly performed with longitudinal waves of 10 MHz during the cooling from RT to 130 K at a constant rate of 1 K/min to avoid thermal gradients in the sample and always maintaining the sample near thermal equilibrium. Then, the ultrasonic measurements were **performed** in similar cooling-heating cycles, at **5 and 10 MHz**.

3. Results and discussion

3.1. *Structural, microstructural, and thermal analyses characterizations*

It was confirmed the chemical composition of the as-received Ni–Ti samples from XRF (Table 1). The Ni content was in good agreement with the nominal composition, while some impurities, such as Fe, were slightly higher than the supplier chemical data.

Fig. 1 shows the XRD pattern and Rietveld refinement results for Ni–Ti sample at RT for as-received and after ultrasonic measurement conditions, where it can be qualitatively

Table 1 – Chemical analysis of the as-received Ni–Ti sample.

Element	Content (wt.%)	Content (at.%)
Ni	57.71 ± 0.05	52.68 ± 0.05
Ti	41.90 ± 0.05	46.90 ± 0.05
Fe	0.10 ± 0.01	0.10 ± 0.01
Balance/Others	0.29 ± 0.01	0.32 ± 0.01

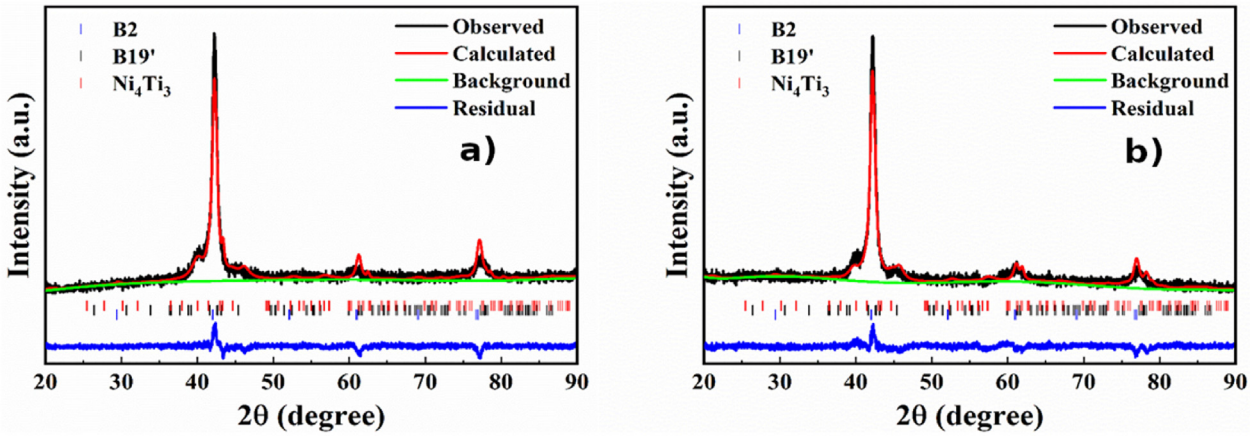

Fig. 1 – XRD pattern and Rietveld refinement results for as-received Ni–Ti sample with the coexistence of austenite (B2), martensite (B19′), and Ni_4Ti_3 phases: (a) as-received and (b) after ultrasonic measurement conditions.

observed at the most intense diffraction peak (2θ ~ 42°), two shoulders at higher (2θ ~ 45°) and lower (2θ ~ 40°) diffraction angles, which are associated with the presence of other crystalline phases. Following the literature [39–43], the presence of the diffraction peaks around the most intense peak at 2θ ~ 42° in Ni–Ti alloys could be related to the Ni_4Ti_3 (trigonal, R $\bar{3}$) for high diffraction angles and with B19' martensite phase (monoclinic, $P2_1/m$) for both low and high angles, which coexist with B2 austenite phase (cubic, Pm $\bar{3}$ m). The best Rietveld refinement results, with excellent convergence and stability, was achieved considering the coexistence of austenite B2 (ICSD 105412), martensite B19' (ICSD 164156), and Ni_4Ti_3 (ICSD 105422) phases. The Rietveld refinement (GoF <2.000) indicated the presence of a majority of austenite B2, with some amount of martensite B19' (~30%), and minor Ni_4Ti_3 (>20%) phases in both conditions.

The microstructural features of the Ni–Ti sample are shown in Fig. 2 for as-received condition. The microstructure, Fig. 2a and b, is composed of a biphasic morphology, with some grains of the austenite B2 phase permeated by needle-like structures of the martensite B19' phase. The Ni_4Ti_3 phase could not be identified through SEM images due to its low volumetric fraction in the microstructure, in agreement with the Rietveld refinement results. The irregular austenite grain size is also a result of the thermomechanical processing of the sample. The chemical mapping, Fig. 2c–e, indicates that the small inclusions, with length in the order of tens of micrometers, presented in the microstructure were slightly Ni-depleted, which could be related to Ti-rich oxides particles formed during the thermomechanical processing. Fig. 2c–e presents X-ray elemental mapping through EDS of Ti–K (blue) in Fig. 2d and Ni–K (red) in Fig. 2e.

The semi-quantitative microanalysis of the as-received Ni–Ti sample was performed by EDX with ZAF correction (EDAX ZAF), being the obtained results presented in Table 2. Similar to the XRF composition, the sample exhibited a Ni-rich content, indicating a uniform elemental distribution at the micrometric level.

Thermal characterization through DSC analysis of the as-received Ni–Ti sample (Fig. 3) was employed to determine the endothermic and exothermic processes that arise from the martensitic phase transformations. The DSC curve obtained during the heating of the as-received Ni–Ti sample **shows** two endothermic events, between **250 and 300 K**, which should be related to the B19' to R-phase transformation (273.9 K), and to R-phase to austenite B2 phase (291.2 K), respectively, as shown in the inset of Fig. 3. Upon cooling, the DSC **present** complex exothermic reaction peaks in the range of the RT to 270 K, which should be associated with the austenite B2 to R-phase transition (B2 → R). Additionally, a sizeable exothermic event, with low intensity, was also detected during the cooling cycle, between **180 and 170 K**, centered at 176.1 K, which could be related to the pre-martensite R-phase to martensite phase transition (R → B19'). Therefore, the sequence of phase transformations, B2 → R → B19', detected during the cooling cycle is evidenced in the two-stage symmetrical martensite transition [44,45]. Wang et al. [46] reported that only the B2 → B19' transformation could be observed in the full solution annealed binary Ni–Ti alloys.

The occurrence of Ni_4Ti_3 precipitates in the Ni–Ti sample already in as-received condition at RT, as observed in XRD analysis can be strictly related to the thermomechanical treatment history of this alloy. In this sense, the absence of DSC events related to the precipitation of intermetallic phases is expected. Also, the presence of small content of a third alloying element, such as Fe and Al, in polycrystalline Ni–Ti alloys can favor R-phase formation [15,39]. Moreover, the pre-martensite R-phase presence already on its early formation stages shows a significantly rhombohedral distortion of this phase which further increases with decreasing temperature [47].

On the other hand, precipitates (such as Ni_4Ti_3) or dislocations, which can be introduced by various thermomechanical treatments, are essential for inducing the R-phase transformation [31,48]. Thus, the existence of DSC peaks associated with the pre-martensite R-phase is a good indication of precipitates and/or dislocations in the sample microstructure. Bataillard et al. [49] used "in situ" TEM analysis to study the microstructural evolution of Ni–Ti alloys during the

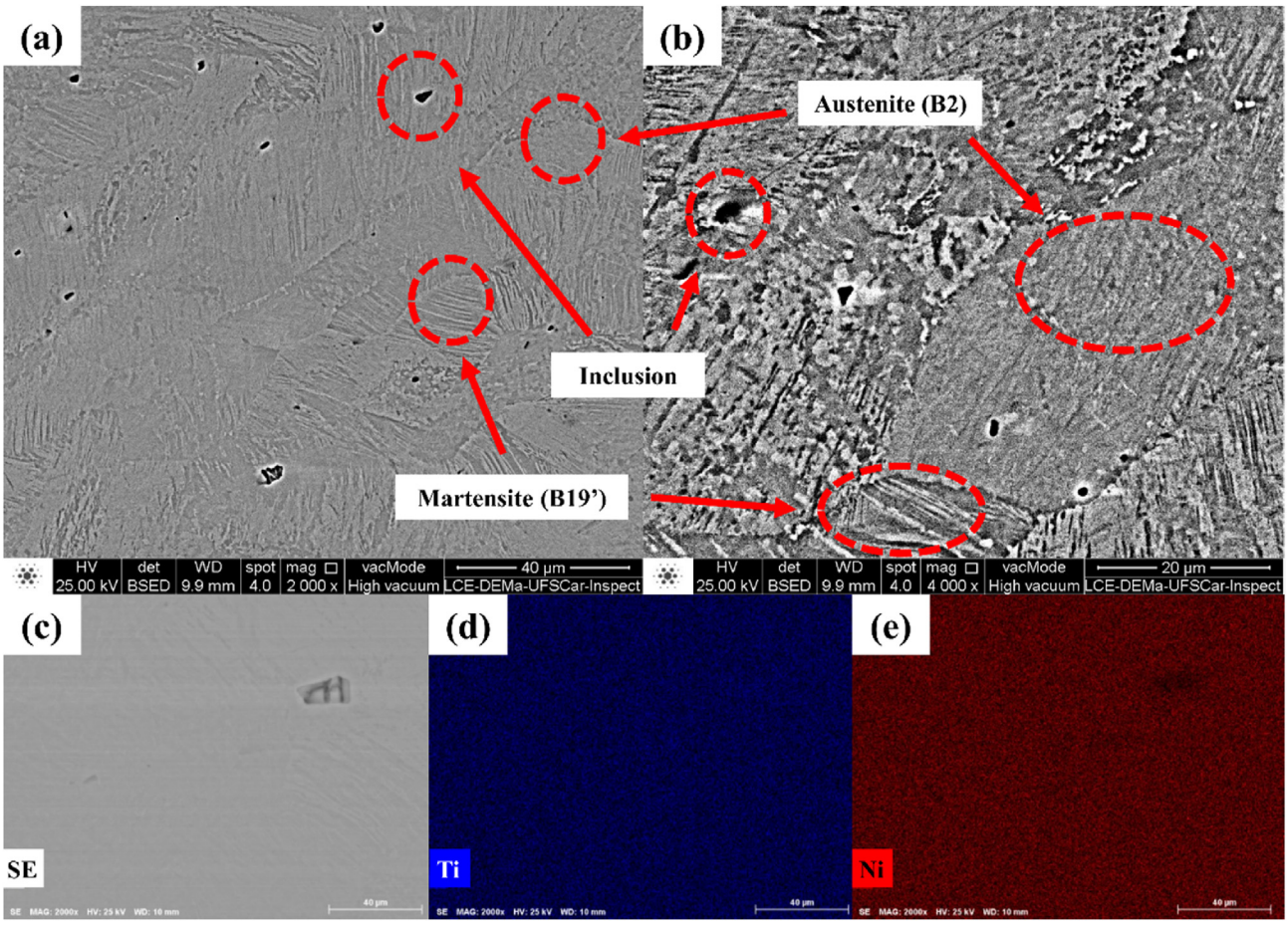

Fig. 2 – SEM/EDS analysis of the as-received Ni–Ti sample: (a) and (b) imaging of the austenite and martensite phases; (c), (d), and (e) X-ray elemental mapping through EDS of Ti–K (blue) and Ni–K (red).

R-phase transformation into martensite. At the starting temperature, the crystalline structure was identified as a single austenite B2 phase containing Ni_4Ti_3 precipitates, which acts as the source of a local stress field, influencing the nucleation and the growth of the R and martensitic phases. The R-phase nucleation occurs around the Ni_4Ti_3 intermetallic, and it shows a triangular morphology. Simultaneously, the martensite phase grows with a preferred orientation due to the precipitates' stress field, which appears in a needle or lamellar shape nucleating from the precipitates towards the bulk. As observed in the DSC curve (Fig. 3) during the cooling cycle, a significant separation (around 100 K) was detected between the temperatures for B2 → R and R → B19' phase transitions. As was reported by Sitepu [39], a small Fe addition in Ni-rich Ni–Ti alloys should spread the temperature ranges for B2 → R and R → B19' transformation by more than 100 K. Thus, the observed behavior in DSC data for the temperature range between phase transitions in as-received Ni–Ti alloy can be associated with the alloying elements impurities found in the studied alloy. The Fe impurity fraction should be highlighted, which agrees with XRF analysis (see Table 1), at least twice the value reported by the supplier in the nominal chemical composition.

The TEM analysis was required in order to confirm the phases formed after cryogenic cooling-heating cycles for the ultrasonic velocity and attenuation measurements, expecting that no significant phase transformation would occur after such treatment.

Fig. 4 presents TEM bright field image at lower magnification of NiTi alloy showing in Fig. 4a the general microstructure with grain size of hundreds of nanometers (sub-micron grains). In the right upper corner of Fig. 4a it is presented the selected area diffraction (SAD) of $[0\ 0\ 1]_{NiTi}$ zone axis. Fig. 4b shows TEM-BF image of another region of microstructure with NiTi cubic (B2) matrix and Ni_4Ti_3 precipitate (red dotted circle), with respective SAD of NiTi phase (white square - right upper

Table 2 – EDS semi-quantitative microanalysis through SEM of an as-received Ni–Ti sample.

Element	Content (wt.%)	Content (at.%)	K-Ratio	Z	A	F
Ti–K	44.5	49.6	0.4357	0.9875	0.9590	1.0337
Ni–K	55.5	50.4	0.5346	1.0091	0.9546	1.0000

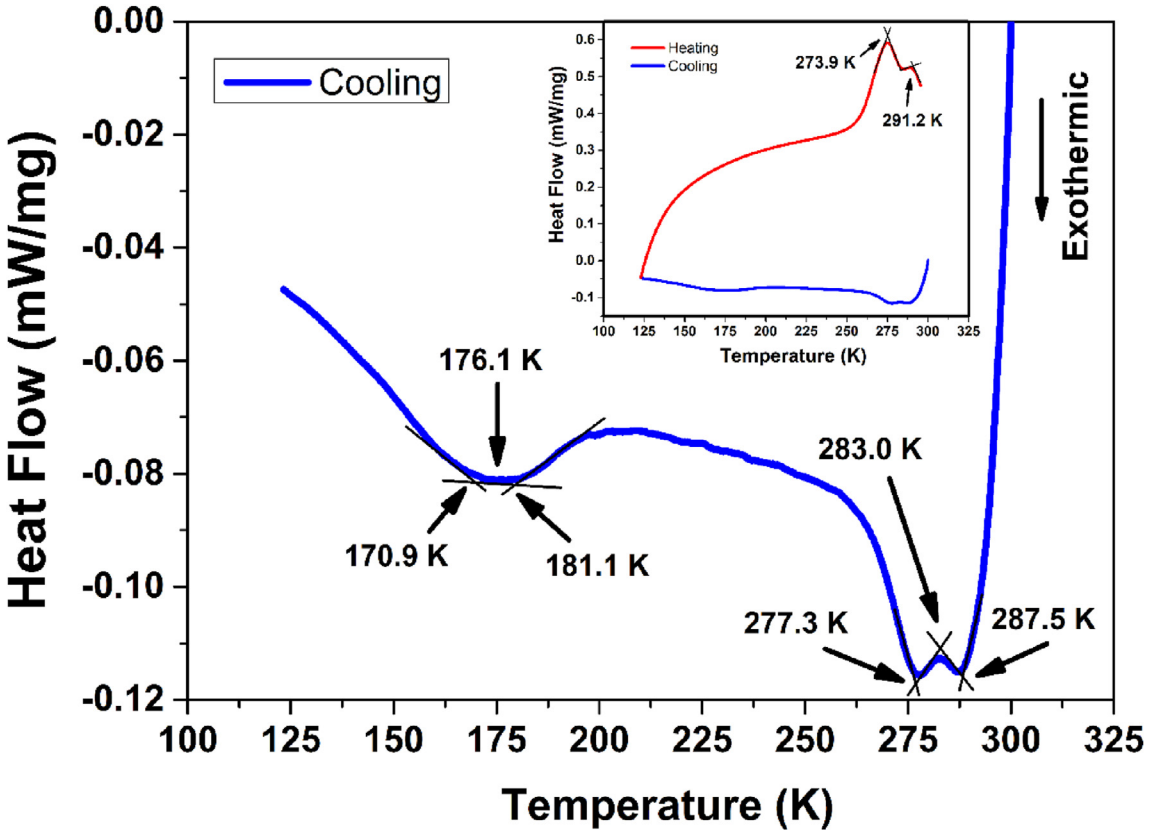

Fig. 3 – DSC curve of the as-received Ni–Ti sample.

corner), and SAD of Ni_4Ti_3 intermetallic phase (red square – left lower corner) in the $[3\ 1\ 1]_{Ni4Ti3}$ zone axis.

In order to confirm composition of phases in the microstructure of NiTi alloy it was realized the **scanning transmission electron microscopy (STEM) image mode combined with EDS analysis**. Fig. 5 presents **STEM-annular dark field (ADF)** micrograph of NiTi alloy showing NiTi cubic (B2) grains and darker precipitate (Fig. 5a). Fig. 5b and c presents respective X-ray elemental mapping through STEM-EDS **showing: (i) Ni–K; and (ii) Ti–K distributions**, confirming uniform distribution of elements at nanoscale in the NiTi matrix and the existence of Ni_4Ti_3 intermetallic phase. These TEM results are in agreement with the XRD patterns and crystalline phases previously identified in the microstructure characterization.

3.2. *Ultrasonic attenuation analysis at low temperatures*

Ultrasonic velocity and attenuation measurements were carried out to obtain additional information about the temperature dependence of phase transitions and the anelastic relaxations between them in an as-received Ni-rich polycrystalline Ni–Ti alloy. Fig. 6 shows the 10 MHz ultrasonic attenuation and velocity measured for the as-received Ni–Ti sample during cooling in the **295 to 130 K** temperature range. A highly complex attenuation spectrum response was observed, associated with some anomalies in velocity.

In order to facilitate the comparison with DSC characterization (see Fig. 3) and previous works available in the literature for different compositions of Ni–Ti alloys [18,30,32,50,51], the anelastic relaxation spectrum (Fig. 6) was divided into four temperature regions, labeled as $T_{A\rightarrow R}$, R, $T_{R\rightarrow M}$, and M. At RT, the austenite B2 is the majority phase in the Ni–Ti alloy in this study. Starting the cooling, the beginning of the anomalous attenuation increased due to internal changes in the material. In the $T_{A\rightarrow R}$ temperature range, where the austenite B2 → R transition takes place, there were identified three ultrasonic attenuation anomalies, labeled as P1, P2, and P3. These anomalies should be related to the austenite to R-phase transformation, extending until 234 K when the wave velocity reaches a minimum value. The R temperature region, where the R-phase is the majority phase is expected, presented two ultrasonic anomalies, P4 and P5, where the R-phase majority fraction is expected. The $T_{R\rightarrow M}$ temperature range is compatible with the corresponding R-phase to martensite B19' phase transformation observed in the DSC curve. This phase transformation is identified as the attenuation peak, P1', followed by an abrupt wave velocity anomalous decrease. In the last temperature range, M, where a majority (or a single) martensite B19' phase is expected, an attenuation anomaly P2' is observed. Due to these anelastic anomalies' complex nature, the identification and interpretation of the physical mechanism responsible for each attenuation peak will be independently treated, as follows.

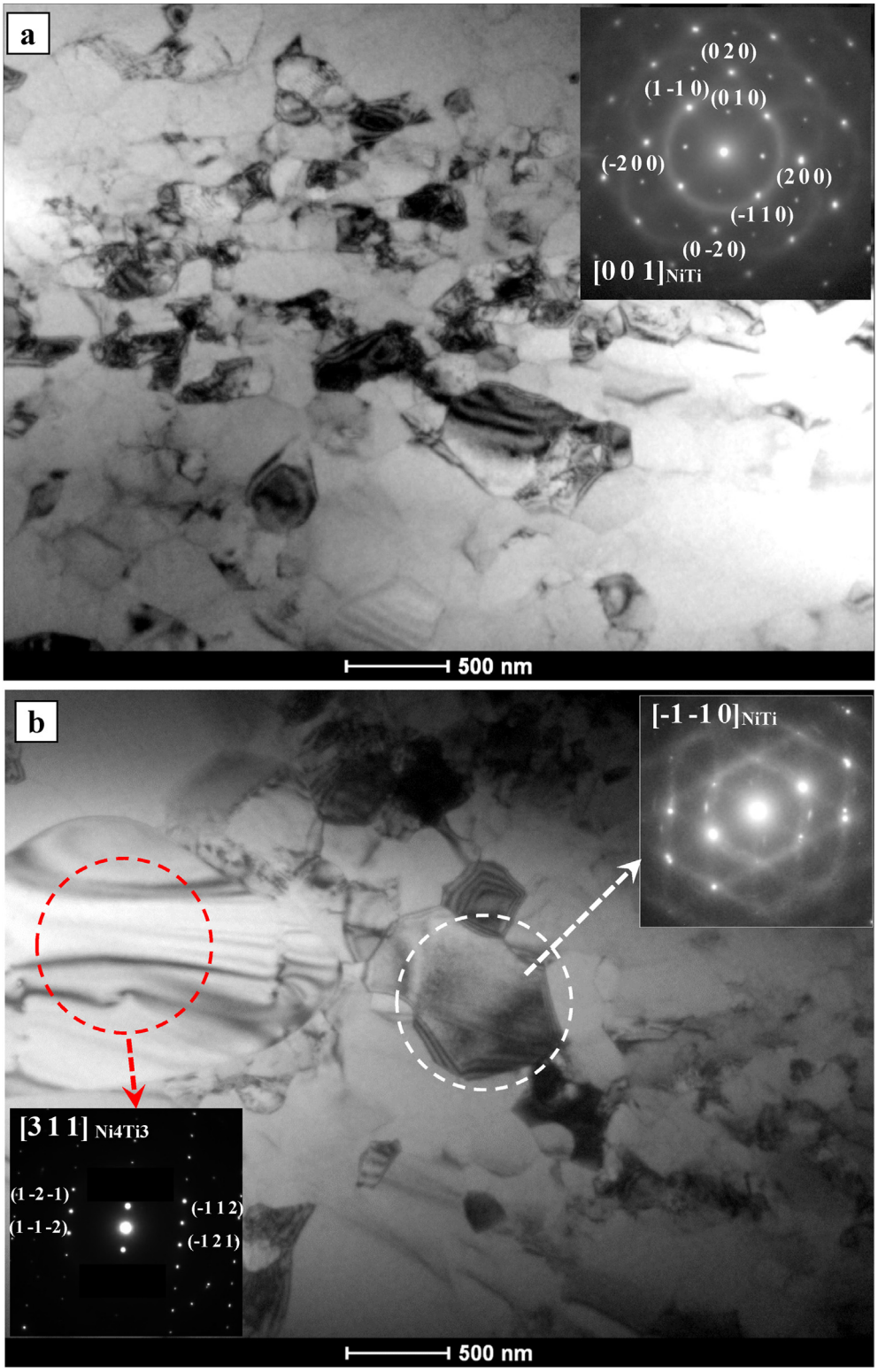

Fig. 4 – TEM bright field image of NiTi as-cast alloy at lower magnification showing (a) general microstructure with grain size of hundreds of nanometers (sub-micron grains). (b) TEM bright field image of NiTi as-cast alloy showing (a) NiTi cubic (B2) matrix and Ni_4Ti_3 precipitate (red dotted circle), selected area diffraction (SAD) of Ni-fcc matrix (white square), and SAD of Ni_4Ti_3 intermetallic phase (red square).

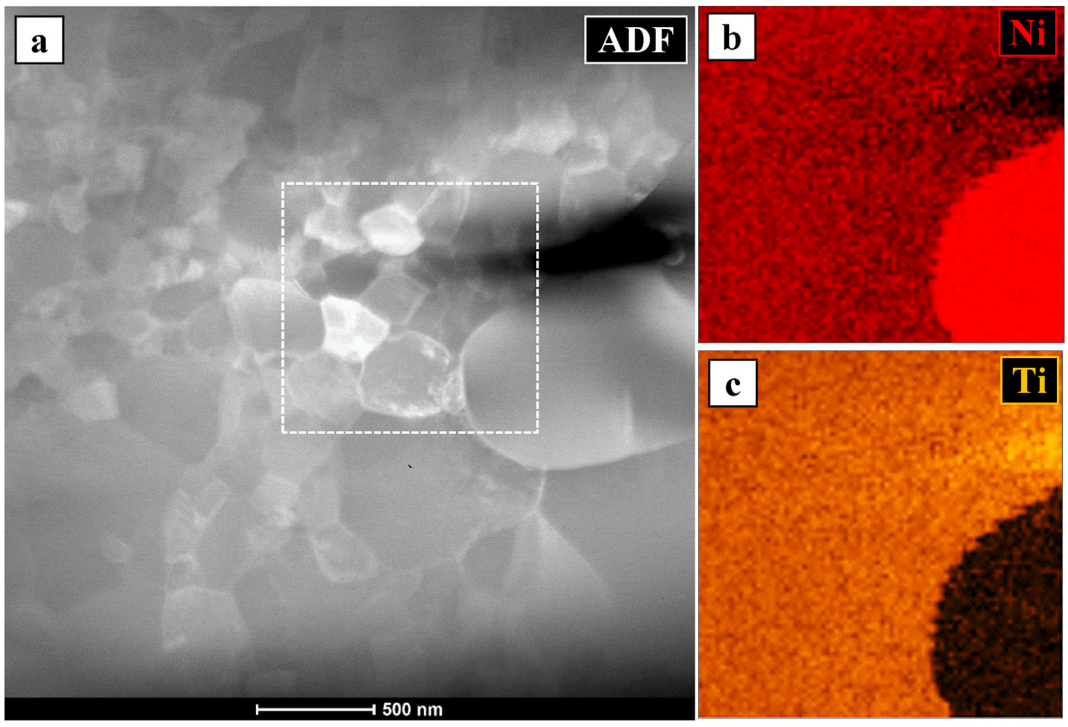

Fig. 5 – (a) STEM-ADF (annular dark field) image of NiTi as-cast alloy showing NiTi cubic (B2) grains and darker precipitate at the right and respective X-ray elemental mapping through EDS showing: (b) Ni–K; and (c) Ti–K distributions, confirming uniform distribution of elements (dotted white line region of Fig. 5a) of matrix and Ni_4Ti_3 intermetallic phase.

3.2.1. P1, P2, and P3 peaks

Fig. 7a shows the ultrasonic velocity dependence with temperature decreasing in the $T_{A\rightarrow R}$ region around P1, P2, and P3 ultrasonic attenuation anomalies at a frequency of 10 MHz. Fig. 7b presents the ultrasonic attenuation response observed at a longitudinal wave with **5 and 10 MHz** frequencies. The latter was measured after five thermal cooling-heating at RT cycles for temperatures around P1, P2, and P3 peaks.

Figs. 6 and 7, it is observed for 10 MHz a sharp and strong attenuation peak, labeled as P1, at temperatures around 280 K,

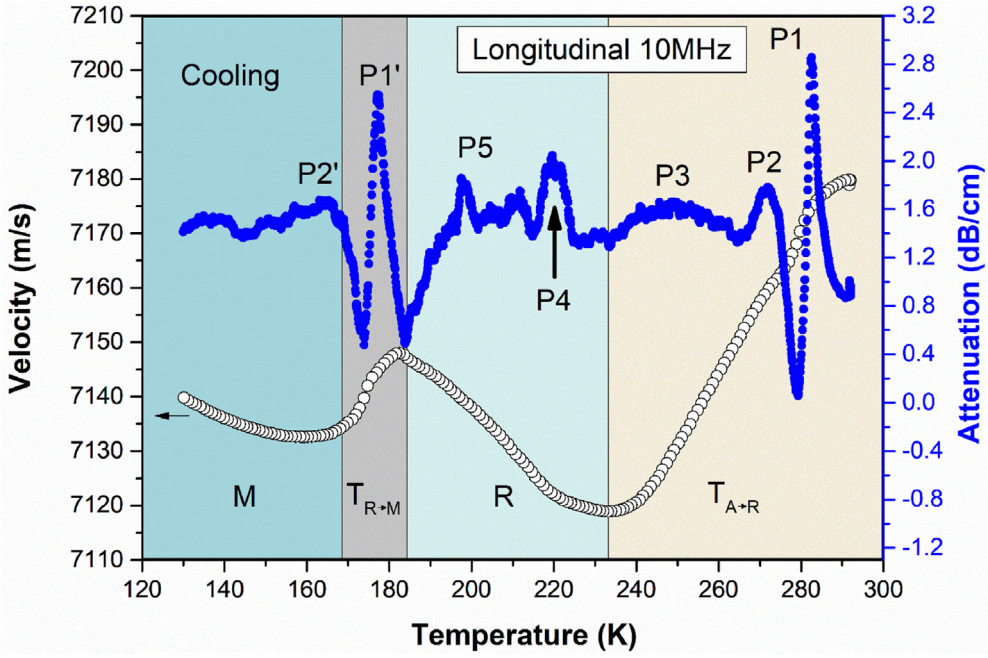

Fig. 6 – 10 MHz longitudinal ultrasonic velocity and attenuation for as-received Ni–Ti alloy measured in the temperature interval 130 K–295 K during cooling.

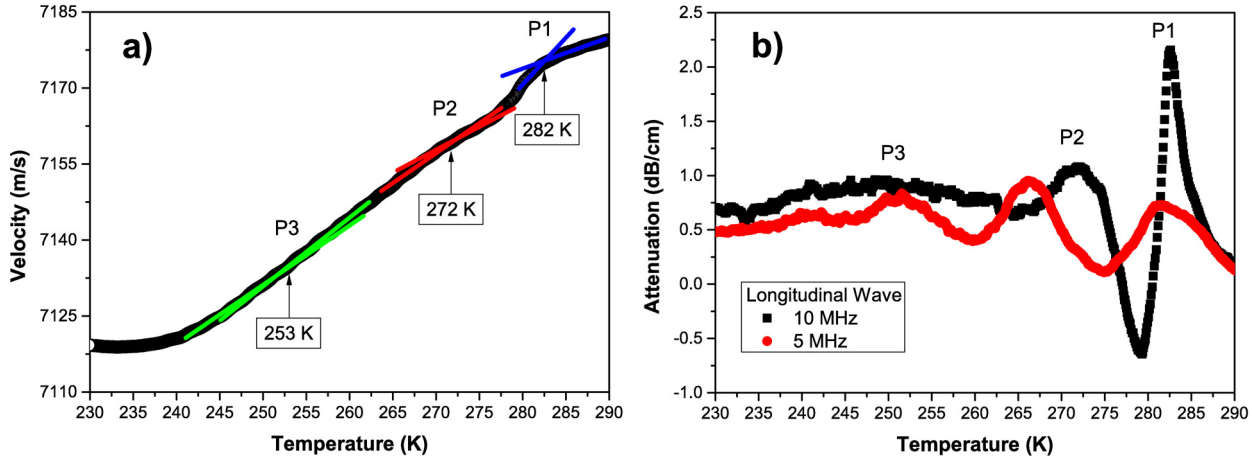

Fig. 7 – (a) Ultrasonic velocity as a function of temperature for as-received Ni–Ti alloy measured with longitudinal waves of 10 MHz during cooling, around P1, P2, and P3 anomalies (see Fig. 6), and (b) ultrasonic attenuation as a function of temperature measured with longitudinal waves of 5 and 10 MHz during cooling. In (a) blue, red, and green lines indicate changes in the linear regime.

accompanied by an abrupt decrease in the corresponding wave velocity (Fig. 7a). The measured ultrasonic velocity changes are directly related to variations of the effective elastic modulus [20]. As observed in Fig. 7b, the P1 peak temperature is frequency-independent for ultrasonic longitudinal waves in the 5–10 MHz range, indicating the structural modification in Ni–Ti alloy. The DSC curve obtained for Ni–Ti alloy during cooling (Fig. 3) shows an endothermic peak associated with B2 → R phase transformation at a similar temperature of the P1 anomaly in ultrasonic characterization. Besides, the P1 peak shape is narrow and asymmetrical and is followed by an abrupt reduction in velocity around 282 K (Fig. 7a), which confirms the phase transition nature of this peak. The ultrasonic velocity curve during cooling did not exhibit an inversion of reduction tendency at the P1 temperature range, but only for temperatures around 230 K. However, the P1 peak should indicate only the beginning of a continuum B2 to R-phase transformation, which can extend to temperatures near the minimum value of elastic modulus (velocity).

Also observed in Figs. 6 and 7, in temperatures around **280 and 270 K**, the attenuation spectrum showed a strong increase in the losses, with a maximum height at 272 K (in 10 MHz), with a subsequent attenuation decreasing until 265 K, denoting an attenuation peak, labeled as P2. Besides, in the P2 peak temperature, the ultrasonic velocity curve at 10 MHz presented an inflection point, as shown in Fig. 7a. The frequency dependence of the P2 anomaly is observed in Fig. 7b, where the P2 peak maximum height was shifted to low temperatures (266 K) due to the reduction of the ultrasonic frequency to 5 MHz, which is compatible with the thermally activated anelastic relaxation mechanisms.

Reducing the temperature, after the P2 anomaly, the ultrasonic attenuation response at 10 MHz, presented a broad anelastic peak, so-called P3, for a temperature range between **230 and 260 K**, and centered around 250 K, which is followed by a weak modification of the wave velocity inclination (Figs. 6 and 7a). The attenuation spectrum of the Ni–Ti sample obtained for longitudinal waves, with a frequency of 5 MHz, showed an unclear frequency-dependence of the P3 peak compared with the ultrasonic characterization results of 10 MHz (Fig. 7b). This fact suggests that the anelastic relaxation mechanism responsible for P3 anomaly is weakly frequency-dependent, or near frequency-independent, for ultrasonic longitudinal waves over this range. After the P3 maximum, the ultrasonic attenuation reduction related to the P3 occurs at the same temperature range when the wave velocity curve reaches its minimum value and inflection point (Figs. 6 and 7a). This fact should be associated with the end of the diffuse phase transition between austenite B2 and pre-martensite R-phase.

Although in a different frequency range, about 1 Hz, Bührer et al. [50] studied the structural evolution of the Ni-rich Ni–Ti alloy. In the reported anelastic relaxation characterization, they detected two wide, and asymmetrical internal friction peaks during the sample cooling, centered at **270 and 190 K**. Those peaks were associated with the austenite to pre-martensite R-phase and R-phase to the martensite phase transformations, respectively.

Golovin et al. [51] studied the mechanisms of dislocation–impurities interaction in the B2 and martensite phases in Ti-50.6 at.%Ni alloys, submitted to plastic deformation and distinct heat treatments, using internal friction measurements at Hz frequencies during cooling. The reported internal friction spectrum was composed of two narrow peaks, at **285 and 220 K**, related to B2 → R and R → B19', respectively.

Matsumoto and Ishiguro [30] analyzed the ultrasonic attenuation response of the high purity equiatomic Ni–Ti alloy using longitudinal waves at 10 MHz in temperatures around the martensite transition. It was reported two attenuation peaks observed during cooling, a sharp peak at 253 K caused by the transition from the high-temperature phase (CsCl structure) to the intermediate phase (rhombohedral), and a broad and asymmetric peak at about 203 K during the martensitic transformation on cooling. However, the analysis data from Matsumoto and Ishiguro [30] detected that the

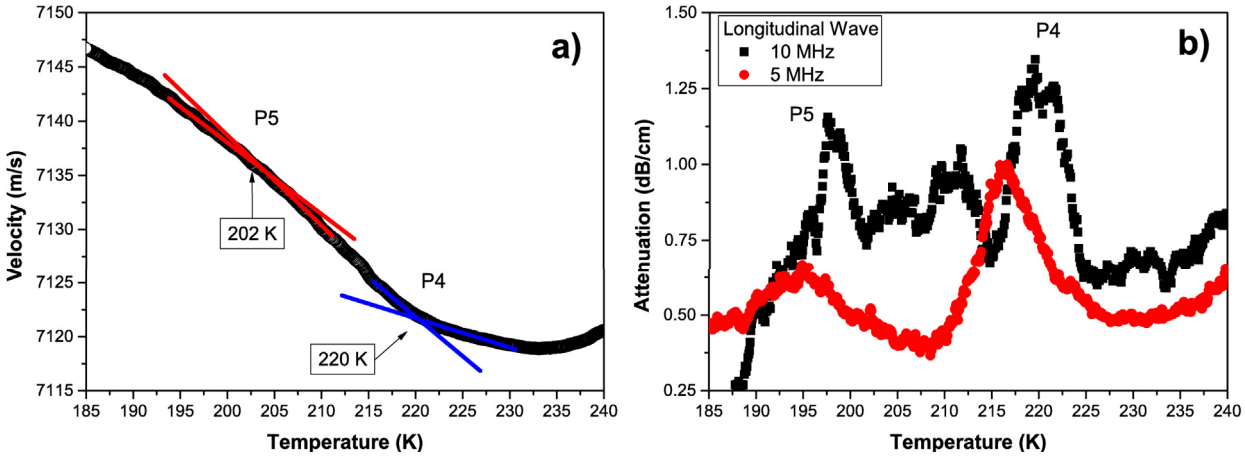

Fig. 8 – (a) Ultrasonic velocity as a function of temperature for as-received Ni–Ti alloy measured with longitudinal waves of 10 MHz during cooling, around P4 and P5 anomalies (see Fig. 6), and (b) ultrasonic attenuation as a function of temperature measured with longitudinal waves of 5 and 10 MHz during cooling. The blue and red lines are an indication of linear regime changes.

broad and asymmetric peak around 203 K reported is, in fact, separated into two peaks, at **220 and 200 K**.

Ren et al. [32] reported ultrasonic attenuation experiments on a single crystal of $Ni_{50}Ti_{50}$ using [001] longitudinal waves with a frequency of 30 MHz during cooling. Around the B2–B19' phase transition, they reported an ultrasonic attenuation spectrum composed of three peaks. The two first peaks (P1+P2) are convoluted, centered at 268 K, and the third attenuation is a broad peak (P3) centered at 252 K. According to systematic studies, the P1 peak was related to the B2–B19' phase transition. In contrast, the P2 peak was associated with a drastic evolution of martensite domains (phase boundaries and martensite twin boundaries) during the martensite phase growth. It lowered the temperature correspondingly to observations of the coarsening of ferroelastic domains in second-order phase transitions. P3 was also related to martensite twin boundary motion.

The P1 and P2 attenuation peaks convolution in an equiatomic single crystal of Ni–Ti proposed by Ren et al. [32] was directly related to a wide temperature interval of the first-order martensite phase transition occurrence, then both processes concur in this two-phase region. For second-order ferroelastic transformation, P1 and P2 peaks should be separated, as observed in Figs. 6 and 7b.

Wang et al. [46] reviewed the unique properties of R-phase transformations in near-equiatomic NiTi alloys. They reported that the R-phase transformation was characterized as a pre-martensitic transformation, and the thermodynamic order of this phase transformation was extensively treated. In accordance with Wang et al. [46] and their references, the B2 → R phase transition is an independent martensitic transformation created by the rhombohedral distortion of the B2 lattice that occurs before the B19' transformation, and it is mainly considered as a first-order transformation. However, the R-phase also shows second-order transformation behavior, as after the B2 → R transformation, the rhombohedral angle α of the R-phase gradually decreases with decreasing temperature or increasing stress.

On the other hand, following Landau-Devonshire phase transition formalism applied to processes that occur at a structural phase transformation on the quantities measured in ultrasonic experiments [52], the elastic constants curves dependence (which is proportional to velocity wave) around the transition temperature region evidence distinct behavior between first- and second-order phase transitions. For first-order phase transformation, the elastic constants should present an abrupt change in a narrow temperature range, with a minimum value at the transition temperature. In contrast, for continuum phase transitions, the elastic constants should change in a wide range of temperature, which characterizes this transition order's diffuse nature.

Thus, considering that the Ni–Ti alloy under analysis is a commercial Ni-rich polycrystalline Ni–Ti alloy, we can assume that the P1 peak here reported is compatible with the B2 to R-phase transformation. It is worth mentioning that the main differences between the literature data and our observations are related to ultrasonic waves' behavior near the P1 peak, when observed only an abrupt change at 282 K (see Fig. 7a) but without minimum at the P1 peak position. As observed in Fig. 6, the velocity wave curve reaches a minimum value of around 235 K. These facts suggest that the B2 to R-phase transition in this sample has a diffuse characteristic, being that the P1 peak is related to the beginning of this phase transformation. At the same time, the minimum velocity assigns the end of the transition.

The occurrence of the satellite P2 peak separated from the P1 anomaly is in good agreement with the ferroelastic nature, diffuse, and continuum of the B2 to R-phase transformation here reported for a commercial Ni-rich polycrystalline Ni–Ti alloy. As discussed previously, the P2 peak should be intrinsically related to the coarsening of pre-martensite ferroelastic domains in second-order phase transitions, which evidenced

a drastic domain evolution due to the forming and accommodation mechanism of the domain walls in twinned R-phase growth.

Liang et al. [33] extended the ultrasonic measurements in single crystals of $Ni_{50}Ti_{50}$ for [001] longitudinal waves with a frequency of 10 MHz during sample cooling. The authors confirmed that the P1 and P2 peaks separation, and a meaningful low-temperature shift of the Ren's P3 peak, now centered at 240 K. The proposed physical interpretation of the peak at 240 K was similar to the internal friction peak reported by anelastic characterization in Hz range around 200 K in NiTi-type shape memory alloys [53], well-known as part of rather complex damping spectra below the martensitic transition. This peak could be attributed to a Snoek- (or possibly Zener-) type hydrogen relaxation [54].

The weakly frequency-dependent or near frequency-independent behavior of the P3 peak here reported suggests that the physical mechanism responsible for this peak should be unlikely related to Snoek-type relaxation due to light impurities, such as hydrogen. On the other hand, a significant number of the studies related to ultrasonic measurements are limited to single crystal equiatomic Ni–Ti alloys, without significant differences between the R-phase and B19' occurrence temperatures, in opposition to the results here reported for a commercially available Ni-rich Ni–Ti alloy. The impurities contents in the Ni-rich polycrystalline Ni–Ti alloy studied can act as decreasing factor for the twinning boundaries mobility rate in the R-phase for ultrasonic longitudinal waves in the studied frequency range, giving place to a weakly frequency dependence of the P3 peak.

3.2.2. *P4 and P5 peaks*

For the temperatures about **214 and 226 K**, the ultrasonic attenuation spectrum of the as-received Ni-rich Ni–Ti alloy measured with longitudinal waves at 10 MHz presented the fourth anomaly, labeled P4. This anomaly, centered at 220 K, is followed by a substantial elastic hardening with temperature decreasing, as observed in Fig. 8a. The P4 peak is also detected when the attenuation spectrum was obtained with longitudinal waves at 5 MHz. However, its maximum height was weakly shifted to lower temperature values (216 K) in comparison to attenuation data collected at 10 MHz, as shown in Fig. 8b. The small thermally activated response of the P4 peak reveals that the origin of P4 should be associated with a physical mechanism that involves higher energy activations or lower relaxation rates.

According to Blanter et al. [18], twin boundaries are considered a generally very efficient damping source in thermoelastic martensite. In particular in NiTi-type shape-memory alloys, which are also able to absorb hydrogen. Different types of twin boundaries, varying with details of the martensitic transformation (with B2, B19, B19' or R phases) depending on alloy composition and heat treatment, are considered sources of the H-free damping spectra. Such spectra may involve either an almost constant high damping in all the martensitic states or a well-developed (non-relaxation and non-transient) peak at the B2 ↔ B19' transition, as discussed above for the P3 peak. However, hydrogen may actively enhance this "transformation peak" (and at the same time decrease the damping in the low-temperature regime) probably due to a pinning/depinning process, as possible to occur in the P1' and P2' peaks to be discussed in the sequence. In other cases, as for B19' martensite, a very high thermally activated relaxation peak, just slightly below the martensitic transition, can be produced by relatively small amounts of hydrogen. This last peak, with activation energy about 0.6–0.7 eV compared to 0.4 eV for the Snoek-type "200 K peak" mentioned above, has been attributed to an H dragging process similar to the Snoek-Köster relaxation for dislocations [53,55–58].

The rhombohedral distortion arising from the R-phase growth and accommodation mechanism in the as-received Ni–Ti sample can slightly improve the dislocations density in temperatures about 230 K (elastic modulus minimum value). Besides considering the H presence among Ni–Ti alloy's impurities elements in the study, even in small concentrations, we suggested that the P4 peak anelastic relaxation mechanism should be a dislocation relaxation in the presence of interstitial hydrogen atoms trapped at the dislocation. A diffusion-controlled bowing mainly causes this relaxation from dislocation segments, *i.e.*, a coupling of stress-induced dislocation motion and interstitial diffusion. It gives the place an H dragging process similar to the Snoek-Köster relaxation.

For temperature range 184–214 K, the Ni–Ti alloy's ultrasonic attenuation measurement for 10 MHz longitudinal wave showed a broad and asymmetric anomaly, at around 200 K, followed by a substantial attenuation reduction until 184 K, which characterizes the P5 peak, as observed in Fig. 6. A significant elastic hardening was detected in association with the attenuation P5 peak, denoted by an inclination change in the velocity wave curve at 202 K, as shown in Fig. 8a. For ultrasonic attenuation measurements at 5 MHz, the maximum height temperature of the P5 peak was observed at 192 K, which denotes the frequency-dependence behavior. The comparison between 5 and 10 MHz attenuation measurements in the P5 peak temperature range for the commercially available Ni-rich Ni–Ti alloy is presented in Fig. 8b. Meanwhile, as well as the P4 peak, the ultrasonic attenuation response of the P5 peak has not been simultaneously reported in previous ultrasonic measurements in Ni–Ti alloys in literature [18,30,32,33,50,51,53–58].

From the structural viewpoint, the monoclinic martensite B19' phase growing is expected to occur already in temperatures slightly smaller than the R → B19' transformation followed by a rhombohedral R-phase fraction reduction. The competition between distinct structural phases in the Ni–Ti alloys is well-known in literature [39,45,47]. The microstructural evolution related to the martensite B19' phase growth happens similarly to the R-phase previously discussed. The martensite nucleation sites are the precipitates' stressed borders, with a needle or lamellar shape starting from the precipitates towards the bulk [49].

Simon and coauthors [59,60] pointed out that during the formation of martensite B19' in Ni–Ti alloys, the additional cooling cycles provide a burst-like growth of some material regions B19′-needles can be observed in addition to B19′-regions that nucleate and grow promoted by the stress-fields of dislocations. Moreover, they proposed that the stress field of an approaching martensite needle activates an in-grown dislocation segment and generates characteristic narrow

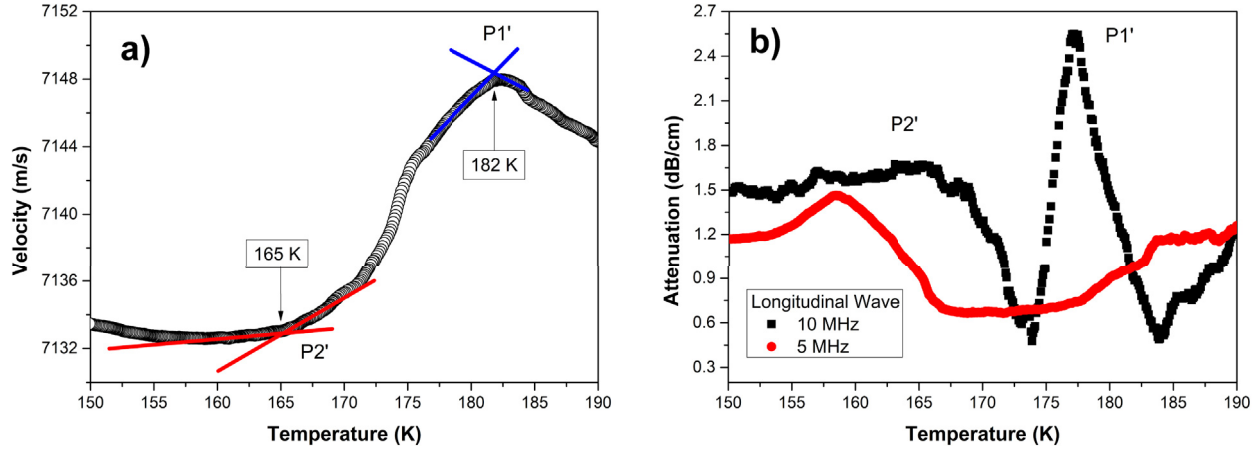

Fig. 9 – (a) Wave velocity as a function of temperature for as-received Ni–Ti alloy measured with longitudinal waves of 10 MHz during cooling, around P1′ and P2′ anomalies, and (b) ultrasonic attenuation as a function of temperature measured with longitudinal waves of 10 and 5 MHz during cooling. The blue and red lines are an indication of linear regime changes.

and elongated dislocation loops that expand along $\{1\ 1\ 0\}_{B2}$ planes parallel to $\{0\ 0\ 1\}_{B19'}$ compound twin planes.

Therefore, due to martensite B19′ phase growth with subsequent R-phase reduction and the structural phases competition around R → B19′ phase transition (below 200 K), the less mobile twinning domain wall of the B19′ phase should be favored over those present in R-phase. This effect increased the elastic modulus hardening with temperature decreasing, followed by reducing the elastic losses, as observed for the P5 peak.

3.2.3. *P1′ and P2′ peaks*

In Fig. 6, for temperatures below 190 K, the ultrasonic attenuation spectrum presents two anomalies, labeled as P1′ and P2′ due to undeniable resemblance to P1 and P2 peaks observed below RT, being P1′ a sharp and asymmetrical peak followed by a satellite P2′ peak. In association with the P1′ peak, centered at 180 K for 10 MHz measurement, the velocity curve (elastic modulus) showed a sudden inflection point, as shown in Fig. 9a, indicating a structural modification in Ni–Ti alloy. As observed in Fig. 3, the DSC curve obtained during cooling of the as-received Ni–Ti alloy showed an intense endothermic reaction peak at approximately the same temperature. This reaction is located at a similar temperature range of the P1′ peak, which should be related to the pre-martensite R-phase (trigonal) to martensite B19′ (monoclinic) phase transformation. The small temperature difference between the DSC curve and ultrasonic attenuation data for R → B19′ phase transition can be associated with the phase transformation kinetics.

Fig. 9b presents the influence of longitudinal wave frequency on the P1′ and P2′ anomalies. It is essential to note the absence of the P1′ peak for ultrasonic measurement at 5 MHz in Fig. 9b. The height of the P1′ peak presented a dependence on the Ni–Ti alloy thermomechanical history, being its value decreased in each new ultrasonic measurement cycle. After about five ultrasonic measurement cycles, the P1′ peak disappeared, and it would not be detected when the frequency was changed to obtain the 5 MHz measurement. The H content in Ni–Ti alloys may actively enhance R → B19′ phase transition, probably due to a pinning/depinning process. Hence, the thermomechanical treatment provided by ultrasonic attenuation measurement cycles can promote a similar effect as thermomechanical aging treatment at low temperatures to the material. This effect was described by Shamini et al. [61], which can give place to decreasing of the H content in solid solution or by the H anchoring by dislocations [22] due to the increase of linear defects density with thermal cycles.

For temperatures below martensite B19′ phase transition (lower than 174 K), as presented in Figs. 6 and 9a, the ultrasonic attenuation curve at 10 MHz showed a typical anelastic anomaly centered at 165 K, labeled as P2′. In Fig. 9a, for temperatures around 165 K, the wave velocity curve presented an indication of linear regime change, compatible with P2' peak, which characterizes a minimum value of the elastic modulus, being recovered the expected hardening elastic modulus behavior with temperature decreasing below P2' peak maximum. Fig. 9b shows the thermally activated behavior of the anelastic mechanism responsible for the P2′ peak, being observed that the P2′ height peak was shifted to a lower temperature (158 K) when the frequency was reduced to 5 MHz.

The separation between P1′ and P2′ is clear evidence of the ferroelastic nature of the martensitic transformation exhibited by the Ni-rich polycrystalline Ni–Ti alloy in the present study. As previously discussed for the P2 peak, the P2′ peak should be intrinsically related to the coarsening of martensite ferroelastic domains in second-order phase transitions, compatible with the domain evolution due to the forming and accommodation mechanism of the twinning boundaries of martensite B19′ phase [32,33,49]. Nevertheless, the main difference between P2 and P2′ peak mechanisms is the less mobile nature of the twinning boundaries of the B19′ phase compared to those of the R-phase. Besides, for low temperatures, the interaction between H and dislocations on the metallic matrix of the Ni–Ti alloys can promote a drastic mobility reduction of the interstitial elements by the freezing (or trapping) mechanism of these impurities, which should be associated with the fast stabilization of the ultrasonic attenuation for temperatures below the P2′ peak.

4. Conclusions

In summary, this work presents a series of ultrasonic characterization, accompanied by XRD, SEM, TEM, and DSC results, of a commercial Ni-rich polycrystalline Ni–Ti alloy (Nitinol). The structural, microstructural, thermal, and thermomechanical properties were used to explore the low-temperature martensitic transformations and shed light on the physical mechanisms which contribute to the complex anelastic relaxation spectrum presented for longitudinal ultrasonic waves during the sample cooling at cryogenic temperatures. The ultrasonic measurements of velocity and attenuation obtained during the Ni–Ti alloy cooling at frequencies of 5 and 10 MHz of longitudinal waves exhibited a complex anelastic spectrum, presenting non-reported evident anomalies below 190 K. The full ultrasonic spectrum is composed of several attenuation peaks identified as phase transitions and anelastic relaxation processes. Several anomalies were detected in our analysis of ultrasonic data, some related to the other experimental techniques and others only from ultrasonics. The ultrasonic characterization from RT below 130 K of Ni-rich polycrystalline Ni–Ti alloy shows the evident anomalies observed below 190 K in ultrasonic attenuation and velocity. The most relevant and not previously reported result in the literature, where two new peaks P1′ and P2′ are observed in Fig. 6. Referred to this figure, the global picture can be established as the P1 and P1′ peaks associated with the beginning of the B2 → R and R→ B19′ phase transitions; in contrast, the main contribution to the satellite P2 and P2′ peaks arises from the twinned R- and B19′-phases domain walls accommodation mechanisms, respectively. The thermal separation observed between P1 and P2, and P1′ and P2′ anomalies agree with the B2 → R and R → B19′ phase transformations' ferroelastic nature. For temperatures 190–260 K, the ultrasonic response showed three relaxation peaks (named P3, P4, and P5) related to complex behavior, such as the twinning boundary mobility of the R-phase, coupling of stress-induced dislocation motion and interstitial diffusion, and increasing less mobile twinning domain wall of the martensite B19′ phase. The ultrasonic results reported and the picture agrees with the complementary techniques, especially to the DSC analysis. Something to highlight is the significant separation (around 100 K) detected between the temperatures for B2 → R and R → B19′ phase transitions, mainly related to impurities in Ni-rich Ni–Ti alloys.

Data availability

The raw/processed data required to reproduce these findings cannot be shared due to technical or time limitations.

Declaration of Competing Interest

The authors declare that they have no known competing financial interests or personal relationships that could have appeared to influence the work reported in this paper.

Acknowledgments

The authors are very grateful for the Brazilian funding agencies for financial support: FAPESP (São Paulo State Research Foundation) grant #2015/50.280-5, CAPES (Coordination for the Improvement of Higher Education Personnel) – Finance Code 001, and CNPq (National Council for Scientific and Technological Development) grant #308.204/2017-4 and #304.073/2019-9, and PEDECIBA, University of the Republic - Ministry of Education and Culture (Program for the Development of Basic Sciences), from Uruguay.

REFERENCES

[1] Sarraf M, Rezvani Ghomi E, Alipour S, Ramakrishna S, Liana Sukiman N. A state-of-the-art review of the fabrication and characteristics of titanium and its alloys for biomedical applications. Bio-Design Manuf 2022;5:371–95. https://doi.org/10.1007/s42242-021-00170-3.

[2] Baltatu MS, Tugui CA, Perju MC, Benchea M, Spataru MC, Sandu AV, et al. Biocompatible titanium alloys used in medical applications. Rev Chim (Bucharest) 2019;70:1302–6. https://doi.org/10.37358/RC.19.4.7114.

[3] Kaur M, Singh K. Review on titanium and titanium based alloys as biomaterials for orthopaedic applications. Mater Sci Eng C 2019;102:844–62. https://doi.org/10.1016/j.msec.2019.04.064.

[4] Nicholson W. J. Titanium alloys for dental implants: a review. Prosthesis 2020;2:100–16. https://doi.org/10.3390/prosthesis2020011.

[5] Williams JC, Boyer RR. Opportunities and issues in the application of titanium alloys for aerospace Components. Metals 2020;10:705. https://doi.org/10.3390/met10060705.

[6] Lei Z, Liu X, Wang H, Wu Y, Jiang S, Lu Z. Development of advanced materials via entropy engineering. Scripta Mater 2019;165:164–9. https://doi.org/10.1016/j.scriptamat.2019.02.015.

[7] Illarionov AG, Nezhdanov AG, Stepanov SI, Muller-Kamskii G, Popov AA. Structure, phase composition, and mechanical properties of biocompatible titanium alloys of different types. Phys Met Metallogr 2020;121:367–73. https://doi.org/10.1134/S0031918X20040055.

[8] Semiatin SL. An overview of the thermomechanical processing of α/β titanium alloys: current status and future Research opportunities. Metall Mater Trans 2020;51:2593–625. https://doi.org/10.1007/s11661-020-05625-3.

[9] Committee F. Specification for wrought nickel-titanium shape memory alloys for medical Devices and surgical implants. ASTM International; 2020.

[10] Miyazaki S, Otsuka K. Development of shape memory alloys. ISIJ Int 1989;29:353–77. https://doi.org/10.2355/isijinternational.29.353.

[11] Jiang H, Cao S, Ke C, Ma X, Zhang X. Fine-grained bulk NiTi shape memory alloy fabricated by rapid solidification process and its mechanical properties and damping performance. J Mater Sci Technol 2013;29:855–62. https://doi.org/10.1016/j.jmst.2013.05.007.

[12] Sun Z, Hao S, Kang G, Ren Y, Liu J, Yang Y, et al. Exploiting ultra-large linear elasticity over a wide temperature range in nanocrystalline NiTi alloy. J Mater Sci Technol 2020;57:197–203. https://doi.org/10.1016/j.jmst.2020.01.073.

[13] Otsuka K, Ren X. Martensitic transformations in nonferrous shape memory alloys. Mater Sci Eng, A 1999;273–275:89–105. https://doi.org/10.1016/S0921-5093(99)00291-9.
[14] Otsuka K, Wayman CM. Shape memory materials. Cambridge University Press; 1999.
[15] Velmurugan C, Senthilkumar V, Dinesh S, Arulkirubakaran D. Review on phase transformation behavior of NiTi shape memory alloys. Mater Today Proc 2018;5:14597–606. https://doi.org/10.1016/j.matpr.2018.03.051.
[16] Pandolfi GS, Martins SC, Buono VTL, Santos LA. Precipitation kinetics of Ti_3Ni_4 and multistage martensitic transformation in an aged Ni–rich Ni–Ti shape memory alloy. J Mater Res Technol 2020;9:9162–73. https://doi.org/10.1016/j.jmrt.2020.06.046.
[17] Otsuka K, Ren X. Physical metallurgy of Ti–Ni-based shape memory alloys. Prog Mater Sci 2005;50:511–678. https://doi.org/10.1016/j.pmatsci.2004.10.001.
[18] Blanter MS, Golovin IS, Neuhäuser H, Sinning H-R. Internal friction in metallic materials, vol. 90. Berlin, Heidelberg: Springer Berlin Heidelberg; 2007. https://doi.org/10.1007/978-3-540-68758-0.
[19] Schaller R, Fantozzi G, Gremaud GM. Mechanical spectroscopy Q-1 2001: with applications to materials science. CH; Enfield, NH: Trans Tech Publications Ltd.; 2001. Uetikon-Zuerich.
[20] Truell R, Elbaum C, Chick BB. Ultrasonic methods in solid state physics. 1st ed. New York, NY: Elsevier; 1969. https://doi.org/10.1016/C2013-0-12565-2.
[21] Moreno-Gobbi A, Zamir G, Eiras JA. Ultrasonic evidence of the existence of two hydrogen Snoek–Köster relaxations in high-purity single crystal copper. Scripta Mater 2007;57:1073–6. https://doi.org/10.1016/j.scriptamat.2007.08.029.
[22] Moreno-Gobbi A, Zamir G, Eiras JA. Ultrasonic investigation of the interaction of hydrogen-dislocations in copper crystals. Mater Sci Eng, A 2011;528:4255–8. https://doi.org/10.1016/j.msea.2011.02.033.
[23] Stenger TE, Trivisonno J. Ultrasonic study of the two-step martensitic phase transformation in Ni_2MnGa. Phys Rev B 1998;57:2735–9. https://doi.org/10.1103/PhysRevB.57.2735.
[24] Mira J, Rivas J, Moreno-Gobbi A, Pérez Macho M, Paolini G, Rivadulla F. Ultrasonic evidence of an uncorrelated cluster formation temperature in manganites with first-order magnetic transition at the Curie temperature. Phys Rev B 2003;68:092404. https://doi.org/10.1103/PhysRevB.68.092404.
[25] Jatti VS, Singh TP. Effect of deep cryogenic treatment on machinability of NiTi shape memory alloys in electro discharge machining. Appl Mech Mater 2014;592–594:197–201. https://doi.org/10.4028/www.scientific.net/AMM.592-594.197.
[26] Kim JW, Griggs JA, Regan JD, Ellis RA, Cai Z. Effect of cryogenic treatment on nickel-titanium endodontic instruments. Int Endod J 2005;38:364–71. https://doi.org/10.1111/j.1365-2591.2005.00945.x.
[27] Kozlick SB. Effect of cryogenic treatment on the mechanical properties of nickel-titanium shape memory alloys. Concordia University; 2014.
[28] Vinothkumar TS, Miglani R, Lakshminarayananan L. Influence of deep dry cryogenic treatment on cutting efficiency and wear resistance of nickel–titanium rotary endodontic instruments. J Endod 2007;33:1355–8. https://doi.org/10.1016/j.joen.2007.07.017.
[29] Vinothkumar T, Rajadurai A, Kandaswamy D, Prabhakaran G. Microstructure of cryogenically treated martensitic shape memory nickel-titanium alloy. J Conserv Dent 2015;18:292. https://doi.org/10.4103/0972-0707.159727.
[30] Matsumoto H, Ishiguro H. Ultrasonic attenuation in NiTi near the martensitic transformation temperature. J Less Common Met 1988;144:L39–42. https://doi.org/10.1016/0022-5088(88)90156-7.
[31] Ren X, Miura N, Zhang J, Otsuka K, Tanaka K, Koiwa M, et al. A comparative study of elastic constants of Ti–Ni-based alloys prior to martensitic transformation. Mater Sci Eng, A 2001;312:196–206. https://doi.org/10.1016/S0921-5093(00)01876-1.
[32] Ren X, Liang XL, Otsuka K, Suzuki T, Shen HM, Wang YN. 30 MHz ultrasonic attenuation of TiNi single crystal associated with B2-B19' martensitic transformation and twin boundaries. J Phys IV 2001;11:Pr8-75–8-79. https://doi.org/10.1051/jp4:2001813.
[33] Liang X, Ren X, Shen H, Wang Y, Otsuka K, Suzuki T. Ultrasonic attenuation study of TiNi and TiNiCu single crystals. Scripta Mater 2001;45:591–6. https://doi.org/10.1016/S1359-6462(01)01068-5.
[34] Delgadillo-Holtfort I, Kaack M, Yohannes T, Pelzl J, Khalil-Allafi J. Ultrasonic investigation of multistage martensitic transformations in aged Ni-rich Ni–Ti shape memory alloys. Mater Sci Eng, A 2004;378:76–80. https://doi.org/10.1016/j.msea.2003.10.331.
[35] Pelton AR, Dicello J, Miyazaki S. Optimisation of processing and properties of medical grade Nitinol wire. Minim Invasive Ther Allied Technol 2000;9:107–18. https://doi.org/10.3109/13645700009063057.
[36] Larson AC, Von Dreele RB. GSAS: general software analysis system manual. 1994.
[37] Toby BH. EXPGUI , a graphical user interface for GSAS. J Appl Crystallogr 2001;34:210–3. https://doi.org/10.1107/S0021889801002242.
[38] Moreno-Gobbi A, Moreno D, Zamir G. Ultrasonic study of structural instabilities in nickel induced by magnetic fields. Mater Res 2008;11:31–5. https://doi.org/10.1590/S1516-14392008000100006.
[39] Sitepu H. Use of synchrotron diffraction data for describing crystal structure and crystallographic phase Analysis of R-phase NiTi shape memory alloy. Textures Microstruct 2003;35:185–95. https://doi.org/10.1080/07303300310001634961.
[40] Iijima M, Brantley WA, Guo WH, Clark WAT, Yuasa T, Mizoguchi I. X-ray diffraction study of low-temperature phase transformations in nickel–titanium orthodontic wires. Dent Mater 2008;24:1454–60. https://doi.org/10.1016/j.dental.2008.03.005.
[41] Naji H, Khalil-Allafi J, Khalili V. Microstructural characterization and quantitative phase analysis of Ni-rich NiTi after stress assisted aging for long times using the Rietveld method. Mater Chem Phys 2020;241:122317. https://doi.org/10.1016/j.matchemphys.2019.122317.
[42] Shi XB, Guo FM, Zhang JS, Ding HL, Cui LS. Grain size effect on stress hysteresis of nanocrystalline NiTi alloys. J Alloys Compd 2016;688:62–8. https://doi.org/10.1016/j.jallcom.2016.07.168.
[43] Burow J, Frenzel J, Somsen C, Prokofiev E, Valiev R, Eggeler G. Grain nucleation and growth in deformed NiTi shape memory alloys: an in situ TEM study. Shape Mem Superelasticity 2017;3:347–60. https://doi.org/10.1007/s40830-017-0119-y.
[44] Chrobak D, Stróż D. Two-stage R phase transformation in a cold-rolled and annealed Ti-50.6at.%Ni alloy. Scripta Mater 2005;52:757–60. https://doi.org/10.1016/j.scriptamat.2004.12.010.
[45] Duerig TW, Bhattacharya K. The influence of the R-phase on the superelastic behavior of NiTi. Shape Mem Superelasticity 2015;1:153–61. https://doi.org/10.1007/s40830-015-0013-4.

[46] Wang XB, Verlinden B, Van Humbeeck J. R-phase transformation in NiTi alloys. Mater Sci Technol 2014;30:1517–29. https://doi.org/10.1179/1743284714Y.0000000590.
[47] Lukáš P, Šittner P, Lugovoy D, Neov D, Ceretti M. In situ neutron diffraction studies of the R-phase transformation in the NiTi shape memory alloy. Appl Phys Mater Sci Process 2002;74:s1121–3. https://doi.org/10.1007/s003390101201.
[48] Miyazaki S, Otsuka K. Deformation and transition behavior associated with the R-phase in Ti-Ni alloys. Metall Trans A 1986;17:53–63. https://doi.org/10.1007/BF02644442.
[49] Bataillard L, Bidaux J-E, Gotthardt R. Interaction between microstructure and multiple-step transformation in binary NiTi alloys using in-situ transmission electron microscopy observations. Philos Mag A 1998;78:327–44. https://doi.org/10.1080/01418619808241907.
[50] Bührer W, Gotthardt R, Kulik A, Mercier O. Neutron diffraction measurements in equiatomic NiTi - alloys. J Phys Colloq 1982;43:C4-219–4-224. https://doi.org/10.1051/jphyscol:1982428.
[51] Golovin IS, Batajyard L, Shinaeva EV. Mechanism of dislocation-impurity interaction in B2-phase of titanium nickelide and kinetics of diffusionless B2-phase transformation in cooling. Met 1997:78–90.
[52] Rehwald W. The study of structural phase transitions by means of ultrasonic experiments. Adv Phys 1973;22:721–55. https://doi.org/10.1080/00018737300101379.
[53] Coluzzi B, Biscarini A, Mazzolai G, Mazzolai FM. A new low-temperature internal friction peak in NiTi based alloys. Mater Sci Eng, A 2006;442:414–7. https://doi.org/10.1016/j.msea.2006.03.125.
[54] Mazzolai FM, Coluzzi B, Mazzolai G, Biscarini A. Hydrogen diffusion and interpretation of the 200K anelastic relaxation in NiTi alloys. Appl Phys Lett 2004;85:2756–8. https://doi.org/10.1063/1.1799247.
[55] Biscarini A, Campanella R, Coluzzi B, Mazzolai G, Trotta L, Tuissi A, et al. Martensitic transitions and mechanical spectroscopy of $Ni_{50.8}Ti_{49.2}$ alloy containing hydrogen. Acta Mater 1999;47:4525–33. https://doi.org/10.1016/S1359-6454(99)00337-7.
[56] Biscarini A, Coluzzi B, Mazzolai G, Mazzolai FM, Tuissi A. Mechanical spectroscopy of the H-free and H-doped $Ni_{30}Ti_{50}Cu_{20}$ shape memory alloy. J Alloys Compd 2003;356–357:669–72. https://doi.org/10.1016/S0925-8388(02)01289-6.
[57] Biscarini A, Coluzzi B, Mazzolai G, Tuissi A, Mazzolai FM. Extraordinary high damping of hydrogen-doped NiTi and NiTiCu shape memory alloys. J Alloys Compd 2003;355:52–7. https://doi.org/10.1016/S0925-8388(03)00267-6.
[58] Mazzolai FM, Biscarini A, Campanella R, Coluzzi B, Mazzolai G, Rotini A, et al. Internal friction spectra of the $Ni_{40}Ti_{50}Cu_{10}$ shape memory alloy charged with hydrogen. Acta Mater 2003;51:573–83. https://doi.org/10.1016/S1359-6454(02)00439-1.
[59] Simon T, Kröger A, Somsen C, Dlouhy A, Eggeler G. On the multiplication of dislocations during martensitic transformations in NiTi shape memory alloys. Acta Mater 2010;58:1850–60. https://doi.org/10.1016/j.actamat.2009.11.028.
[60] Simon T, Kröger A, Somsen C, Dlouhy A, Eggeler G. In-situ TEM cooling/heating experiments on deformed NiTi shape memory single crystals. European Symposium on Martensitic Transformations 2009. https://doi.org/10.1051/esomat/200902030.
[61] Shamimi A, Amin-Ahmadi B, Stebner A, Duerig T. The effect of low temperature aging and the evolution of R-phase in Ni-rich NiTi. Shape Mem Superelasticity 2018;4:417–27. https://doi.org/10.1007/s40830-018-0193-9.